NASA Technical Paper 3575

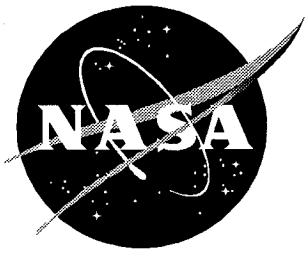

Electromagnetic Scattering Analysis of Arbitrarily Shaped Material Cylinder by FEM-BEM Method

M. D. Deshpande, C. R. Cockrell, and C. J. Reddy

July 1996

NASA Technical Paper 3575

Electromagnetic Scattering Analysis of Arbitrarily Shaped Material Cylinder by FEM-BEM Method

M. D. Deshpande
VIGYAN, Inc. • Hampton, Virginia

C. R. Cockrell and C. J. Reddy
Langley Research Center • Hampton, Virginia

National Aeronautics and Space Administration
Langley Research Center • Hampton, Virginia 23681-0001

July 1996

Available electronically at the following URL address: http://techreports.larc.nasa.gov/ltrs/ltrs.html

Printed copies available from the following:

NASA Center for AeroSpace Information
800 Elkridge Landing Road
Linthicum Heights, MD 21090-2934
(301) 621-0390

National Technical Information Service (NTIS)
5285 Port Royal Road
Springfield, VA 22161-2171
(703) 487-4650

Abstract

A hybrid method that combines the finite element method (FEM) and the boundary element method (BEM) is developed to analyze electromagnetic scattering from arbitrarily shaped material cylinders. By this method, the material cylinder is first enclosed by a fictitious boundary. Maxwell's equations are then solved by FEM inside and by BEM outside the boundary. Electromagnetic scattering from several arbitrarily shaped material cylinders is computed and compared with results obtained by other numerical techniques.

1. Introduction

The problem of electromagnetic scattering determination from an arbitrarily shaped material cylinder is considered in this paper. Electromagnetic scattering from an inhomogeneous material cylinder can be determined by two basic approaches—an integral equation and a differential equation.

In the integral equation approach, a surface integral equation or a volume integral equation may be used. In the surface integral equation formulation, conducting surfaces of a scatterer are replaced by equivalent surface electric currents, whereas material surfaces are replaced by both equivalent surface electric and magnetic currents. Coupled integral equations are then formed by application of appropriate boundary conditions to the different field components that are produced by the equivalent currents. These coupled integral equations are solved by the method of moments for the unknown equivalent currents. Arvas and Sarkar (ref. 1) have analyzed radar cross sections of various two-dimensional structures with the surface integral equation approach.

For a cylinder consisting of inhomogeneous material, the surface integral equation approach does not correctly model the inhomogeneity of the material cylinder. In such cases the volume integral equation formulation is then used to accurately model the inhomogeneous material cylinder. In the volume integral equation formulation, the material cylinder is divided into unit cells. These unit cells may be rectangular bricks or tetrahedral shapes and are small enough so that the field intensity is nearly uniform within each cell. The material cylinder is then assumed to be replaced by an equivalent polarization current flowing in these unit cells. The coupled integral equations, which are formed by application of appropriate boundary conditions to the field produced from the equivalent currents, are then solved by the method of moments. Using the polarization current concept, Richmond (ref. 2) determined scattered field patterns of dielectric cylinders of arbitrary cross-sectional shape. The equivalent current concept has also been used by Sarkar and Arvas (ref. 3) and by Schaubert, Wilton, and Glisson (ref. 4) to analyze electromagnetic scattering by arbitrarily shaped inhomogeneous dielectric bodies. However, the method involves the solution of a fully dense matrix equation, which may require prohibitively large computer memory and long computation time.

In the differential equation approach, the volume of the inhomogeneous scatterer is discretized, and Maxwell's equations in differential equation form are solved. Some advantages of the differential equation approach over the integral equation approach are: (1) a method more convenient for handling complex inhomogeneous scatterers, (2) a method that results in sparse matrix equations, and (3) a method better suited for closed-region problems. However, for open-region problems in electromagnetics, such as radiation and scattering, the volume must be properly truncated with an artificial or fictitious boundary with proper absorbing boundary conditions. The accuracy of results obtained with an artificial boundary with absorbing boundary conditions depends upon boundary locations as well as the order of the boundary conditions.

An alternative approach (known as the hybrid approach) presented in this paper retains the advantages of both differential equation and integral equation approaches. The general procedure for a hybrid technique requires that the scatterer be enclosed by an artificial boundary. Maxwell's equations are then

solved by a differential equation approach such as the finite element method (FEM) inside the artificial boundary and by an integral equation approach in discretized form such as the boundary element method (BEM) outside the artificial boundary. Although use of BEM on and outside the artificial boundary results in a full dense matrix, convergence of an approximate solution to the exact solution is guaranteed without a change in the location of the artificial boundary.

The remainder of the paper is organized as follows. Section 3 contains basic formulation of the problem for FEM and BEM. Scattering amplitudes of a few sample problems are computed by the present technique in section 4. Also in section 4, results obtained by the present method are compared with those obtained by other analytical techniques. The paper is concluded in section 5 with comments on the future scope and extension of the present work.

2. Symbols

A_{IJ}^{e}	(I, J)th element of FEM matrix for eth subdomain
a	cylinder radius; triangle side length
$[B]$	finite element matrix
b	boundary circle radius; triangle base length
C	fictitious boundary curve
$[D]$	sparse matrix
D_{Jp}	(J, p)th element of matrix $[D]$
E_0	amplitude of incident electric field
E_z	Z-axis component of total electric field
$\vec{E}_{\text{in}}$	incident electric field vector
e^{jwt}	time convention
f	frequency, Hz
f_s	E or H scattered far field
$G(.)$	free-space Green's function, where $(.)$ represents appropriate argument
$[G]$	square matrix of order $P \times P$
G_{pq}	(p, q)th element of matrix $[G]$
$[G]^{-1}$	inverse of matrix $[G]$
$[H]$	square matrix of order $P \times P$
H_{pq}	(p, q)th element of matrix $[H]$
$H_1^{(2)}(.)$	Hankel function of first order and second kind
$H_0^{(2)}(.)$	Hankel function of zero order and second kind
H_z	Z-axis component of total magnetic field
H_0	amplitude of incident magnetic field
$\vec{H}_{\text{in}}$	incident magnetic field vector
I, J	integers
J_z^i	equivalent electric current representing incident field
j	imaginary number equal to $\sqrt{-1}$
k_0	propagation constant in free space
m, n	integers

$\hat{n}$	unit normal vector of curve C drawn outward
$\hat{n}_1$	unit normal vector of curve C drawn inward
P	number of nodal points on curve C
p	integer for pth nodal point
$Q_p(\eta)$	piecewise distribution along η direction
q	integer for qth nodal point
$\hat{r}$	unit vector
$T(x, y)$	testing function equivalent to W_I^e
$[U]_C$	column matrix with nodal amplitudes of normal derivative on curve C
U_p	amplitude of normal derivative of ψ_t on curve C
W_I^e	expansion function for Ith node over eth triangular subdomain
(x_1, y_1), (x_2, y_2), (x_3, y_3)	coordinates of three vertices of triangle
(x, y)	variables of rectangular coordinates
$\hat{z}$	unit vector along Z-axis
$\alpha_r(x, y)$, $\beta_r(x, y)$	equal to $\mu_r(x, y)$, $\varepsilon_r(x, y)$, respectively, for TM case; equal to $\varepsilon_r(x, y)$, $\mu_r(x, y)$, respectively, for TE case
$[\Gamma]$	column matrix for nodal amplitude
$[\Gamma]_C$	column matrix for nodal amplitude on curve C
Γ_I	amplitude of ψ_t at Ith node
Δ_p	length of linear segment between p and $p + 1$ nodes on curve C
Δ_{p-1}	length of linear segment between p and $p - 1$ nodes on curve C
δ_{IJ}	Kronecker delta function
$\varepsilon(x, y)$	$\varepsilon_0\varepsilon_r(x, y)$
$\varepsilon_r(x, y)$	relative permittivity at (x, y)
ε_0	permittivity of free space
η	variable along linear segments of curve C
Θ_p	angle between two consecutive linear segments of curve C, deg
$\mu(x, y)$	$\mu_0\mu_r(x, y)$
$\mu_r(x, y)$	relative permeability at (x, y)
μ_0	permeability of free space
(ρ, ϕ)	variables of cylindrical coordinate system
(ρ', ϕ')	source coordinate
σ_{2D}	radar scattering width
$[\Upsilon]_C$	column matrix with nodal amplitudes of incident field on curve C
Υ_q	amplitude of incident field at qth node on curve C
ϕ_{in}	incident angle of electromagnetic wave

ψ_{in}	incident electric or magnetic field scalar
ψ_t	total electric field E_z for TM case; total magnetic field H_z for TE case
ω	angular frequency ($2\pi f$), rad/sec

Abbreviations:

in	incident
TE	transverse electric
TM	transverse magnetic

3. Theory

Consider a material cylinder infinite along the Z-axis and of arbitrary cross section as shown in figure 1. For the purpose of analysis, the scattering structure is divided into regions I and II by contour C. Region II may consist in general of inhomogeneous material with permeability $\mu(x, y)$ and permittivity $\varepsilon(x, y)$. It may also have embedded metallic strips within the material. Region I is free space with permeability μ_0 and permittivity ε_0 surrounding the cylinder. An incident electromagnetic wave is assumed in the direction normal to the axis of the cylinder. Both transverse electric (TE) and transverse magnetic (TM) polarizations are considered, and $e^{j\omega t}$ time convention is assumed.

For TM and TE incidence, respectively, the incident field is given by

$$\left.\begin{aligned} \vec{E}_{in} &= \hat{z}\psi_{in} = \hat{z}E_0 e^{jk_0\rho\cos(\phi-\phi_{in})} \\ \vec{H}_{in} &= \hat{z}\psi_{in} = \hat{z}H_0 e^{jk_0\rho\cos(\phi-\phi_{in})} \end{aligned}\right\} \tag{1}$$

where $E_0 = H_0 = 1$ is the amplitude, ϕ_{in} is the incident angle, and (ρ, ϕ) are the variables of the cylindrical coordinate system. The total field ψ_t inside the region bounded by curve C can be determined from the solution of the source-free scalar wave equation given by

$$\nabla \cdot \left[\frac{1}{\alpha_r(x, y)}\nabla\psi_t\right] + k_0^2\beta_r(x, y)\psi_t = 0 \tag{2}$$

In equation (2) $\alpha_r(x, y)$, $\beta_r(x, y)$, and ψ_t are equal to $\mu_r(x, y)$, $\varepsilon_r(x, y)$, and E_z, respectively, for TM Z-axis excitation and are equal to $\varepsilon_r(x, y)$, $\mu_r(x, y)$, and H_z, respectively, for TE to Z-axis excitation. Multiplication of both sides of equation (2) by a testing function $T(x, y)$ and integration over the cross section of region II yields a weak form of the wave equation (Silvester and Ferrari, ref. 5) as

$$\int\int_{\text{Region II}} T\left\{\nabla \cdot \left[\frac{1}{\alpha_r(x, y)}\nabla\psi_t\right] + \beta_r k_0^2(x, y)\psi_t\right\} dx\, dy = 0 \tag{3}$$

With the use of vector identity

$$\nabla \cdot \left\{T\left[\frac{1}{\alpha_r(x, y)}\nabla\psi_t\right]\right\} = T\nabla \cdot \nabla\left[\frac{1}{\alpha_r(x, y)}\psi_t\right] + \nabla T \cdot \nabla\left[\frac{1}{\alpha_r(x, y)}\psi_t\right] \tag{4}$$

and the divergence theorem, equation (3) can be written as

$$\int\int_{\text{Region II}} \left\{\nabla T \cdot \nabla\left[\frac{1}{\alpha_r(x, y)}\psi_t\right] - k_0^2\beta_r(x, y)T\psi_t\right\} dx\, dy = \oint_C T\nabla\psi_t \cdot \hat{n}\, dc \tag{5}$$

where $\hat{n}$ is a unit vector drawn outwardly to the curve C as shown in figure 1.

To construct an approximate solution of equation (5) by FEM, region II is approximated by a union of triangles as shown in figure 2(a). On the eth triangle ψ_t is represented by a linear combination of functions $W_I^e(x, y)$ as

$$\left.\begin{aligned} \psi_t^e &= \sum_{I=1}^{3} \Gamma_I W_I^e(x, y) \qquad \text{(on } e\text{th triangle)} \\ \psi_t^e &= 0 \qquad\qquad\qquad\quad \text{(otherwise)} \end{aligned}\right\} \tag{6}$$

where

$$W_I^e(x, y) = [1 \; x \; y] \begin{bmatrix} 1 & x_1 & y_1 \\ 1 & x_2 & y_2 \\ 1 & x_3 & y_3 \end{bmatrix}^{-1} \begin{bmatrix} \delta_{I1} \\ \delta_{I2} \\ \delta_{I3} \end{bmatrix}$$

and the Kronecker delta function is defined as $\delta_{IJ} = 0$ for $I \neq J$ and $\delta_{IJ} = 1$ for $I = J$. The amplitudes Γ_1, Γ_2, and Γ_3 are the unknown values of ψ_t at the three vertices of the eth triangle having coordinates (x_1, y_1), (x_2, y_2), and (x_3, y_3), respectively. By Galerkin's method with $T(x, y) = W_I^e(x, y)$ and $J = 1$, 2, and 3, the left side of equation (5) over the eth triangle can be written as

$$\sum_{I=1}^{3} \Gamma_I \iint_e \left\{ \nabla W_J^e \cdot \nabla \left[\frac{1}{\alpha_r(x, y)} W_I{}^e \right] - k_0^2 \beta_r(x, y) W_J^e W_I{}^e \right\} dx \, dy \qquad (J = 1, 2, 3) \tag{7}$$

The previous expression can be written in a matrix form as

$$\begin{bmatrix} A_{11}^e & A_{12}^e & A_{13}^e \\ A_{21}^e & A_{22}^e & A_{23}^e \\ A_{31}^e & A_{32}^e & A_{33}^e \end{bmatrix} \begin{bmatrix} \Gamma_1 \\ \Gamma_2 \\ \Gamma_3 \end{bmatrix} \tag{8}$$

where

$$A_{IJ}^e = \iint_e \left\{ \nabla W_J^e \cdot \nabla \left[\frac{1}{\alpha_r(x, y)} W_I{}^e \right] - k_0^2 \beta_r(x, y) W_J^e W_I{}^e \right\} dx \, dy \tag{9}$$

Now consider a union of two triangles as shown in figure 2(b); an expression corresponding to equation (8) for the union of two triangles can be written as

$$\begin{bmatrix} A_{11}^e & A_{12}^e & A_{13}^e & 0 \\ A_{21}^e & (A_{22}^e + A_{55}^f) & (A_{23}^e + A_{56}^f) & A_{54}^f \\ A_{31}^e & (A_{32}^e + A_{65}^f) & (A_{33}^e + A_{66}^f) & A_{64}^f \\ 0 & A_{45}^f & A_{46}^f & 0 \end{bmatrix} \begin{bmatrix} \Gamma_1 \\ \Gamma_2 \\ \Gamma_3 \\ \Gamma_4 \end{bmatrix} \tag{10}$$

where A_{IJ}^f are determined from equation (9) with superscript e replaced by superscript f and the integration performed over the f triangle. An appropriate alignment of common edges, as indicated in

figure 2(b), is required to assure the correct combination of terms in the matrix equation (10). To ensure continuity of fields across the common edge, $\Gamma_6 = \Gamma_3$ and $\Gamma_5 = \Gamma_2$ were enforced in the derivation of equation (10). With an assembled mesh of all triangles over the surface bounded by curve C, the left side of equation (5) can be written as

$$[B][\Gamma] \tag{11}$$

where the elements of the matrix $[B]$ are obtained from A^e_{mn}, $[\Gamma]$ is the column matrix with elements given by the values of ψ_t at the vertices of triangular elements, $m = 1, 2, 3, ..., N$, $n = 1, 2, 3, ..., N$, and N is the total number of nodes.

To evaluate the contour integration on the right side of equation (5), the normal derivative of ψ_t over curve C is required. To determine the normal derivative of ψ_t on curve C, the following procedure is used.

The boundary curve C is discretized into linear segments as shown in figure 3 and the normal derivative of the function ψ_t on the curve is written as

$$\nabla\psi_t \cdot \hat{n} = \sum_{p=1}^{P} U_p Q_p(\eta) \tag{12}$$

where U_p is the unknown amplitude at pth node on curve C. The function $Q_p(\eta)$ varies linearly with η over the segment as

$$\left.\begin{aligned} Q_p(\eta) &= \frac{\eta}{\Delta_{p-1}} && (0 \le \eta \le \Delta_{p-1}) \\ Q_p(\eta) &= \frac{\Delta_p - (\eta - \Delta_{p-1})}{\Delta_p} && (\Delta_{p-1} \le \eta \le \Delta_p) \end{aligned}\right\} \tag{13}$$

The right side of equation (5) can therefore be written as

$$\oint_C T\nabla\psi_t \cdot \hat{n}\, dc = \sum_{p=1}^{P} U_p \oint_C T Q_p(\eta) d\eta = [D][U] \tag{14}$$

where the elements of matrix $[D]$ are given by

$$D_{Jp} = \oint_C W^e_J Q_p(\eta) d\eta \tag{15}$$

The unknown amplitude U_p is determined as follows. The function ψ_t in region I is obtained by the solution of the inhomogeneous wave equation

$$\nabla^2\psi_t + k_0^2\psi_t = -j\omega\mu_0 J^i_z \tag{16}$$

subject to essential and natural boundary conditions on curve C. These essential and natural boundary conditions are the values of the function and its normal derivative on curve C. In equation (16), J^i_z is the equivalent current source producing the incident field.

To obtain a solution, multiply equation (16) by $G(\rho, \phi; \rho', \phi')$, where $G(.)$ is the free-space Green's function for a line source located at (ρ', ϕ'), and integrate over region I, which gives

$$\int_{\text{Region I}} \int (\nabla^2 \psi_t + k_0^2 \psi_t) G(.)\, dx\, dy = -j\omega\mu_0 \int_{\text{Region I}} \int J_z^i G(.)\, dx\, dy \tag{17}$$

From the scalar Green's theorem

$$\int_{\text{Region I}} \int [G(.)\nabla^2 \psi_t - \psi_t \nabla^2 G(.)]\, dx\, dy = \oint_C G(.) \nabla\psi_t \cdot \hat{n}_1\, dc - \oint_C \psi_t \nabla G(.) \bullet \hat{n}_1\, dc \tag{18}$$

where the unit normal vector $\hat{n}_1$ is shown in figure 1. Equation (17) can then be written as

$$\int_{\text{Region I}} \int \psi_t [\nabla^2 G(.) + k_0^2 G(.)]\, dx\, dy = -j\omega\mu_0 \int_{\text{Region I}} \int J_z^i G(.)\, dx\, dy + \oint_C \psi_t \nabla G \cdot \hat{n}_1\, dc - \oint_C \nabla\psi_t \bullet \hat{n}_1 G\, dc \tag{19}$$

Because $[\nabla^2 G(.) + k_0^2 G(.)] = -\delta(\rho - \rho')\delta(\phi - \phi')/\rho$, $j\omega\mu \int_{\text{Region I}} \int J_z^i G(.)\, dx\, dy = \psi_i$, and $\hat{n}_1 = -\hat{n}$, equation (19) can be written as

$$\psi_t(\rho, \phi) = \psi_i(\rho, \phi) - \oint_C \nabla\psi_t \cdot \hat{n} G(.) d\eta + \oint_C \psi_t \nabla G(.) \cdot \hat{n}\, d\eta \tag{20}$$

The free-space Green's function used in the previous equations is given by

$$G(.) = \frac{1}{4j} H_0^{(2)}\left(k_0 \left|\vec{\rho} - \vec{\rho}'\right|\right) \tag{21}$$

$$\nabla G(.) = \hat{r} \frac{jk_0}{4} H_1^{(2)}\left(k_0 \left|\vec{\rho} - \vec{\rho}'\right|\right) \tag{22}$$

where $H_0^{(2)}(.)$ and $H_1^{(2)}(.)$ are the Hankel functions of the second kind of zero and first order, respectively, and $\hat{r}$ is a unit vector along $\vec{\rho} - \vec{\rho}'$. The function ψ_t on the curve in figure 3 can now be represented by

$$\psi_t = \sum_{p=1}^{P} \Gamma_p Q_p(\eta) \tag{23}$$

where Γ_p is the unknown amplitude of ψ_t at the pth node on curve C. Substitution of equations (12) and (21)–(23) into equation (20) yields

$$\Gamma_q \delta_{qq} = \Upsilon_q + \frac{jk_0}{4} \sum_{p=1}^{P} \Gamma_p \int_C H_1^{(2)}\left(k_0 \left|\vec{\rho}_q - \vec{\rho}'\right|\right) Q_p(\eta) \hat{r} \cdot \hat{n}\, d\eta + \frac{j}{4} \sum_{p=1}^{P} U_p \int_C H_0^{(2)}\left(k_0 \left|\vec{\rho}_q - \vec{\rho}'\right|\right) Q_p(\eta)\, d\eta \tag{24}$$

where Υ_q is the value of incident field at the qth node on curve C. Equation (24) can be written in matrix form as

$$\begin{bmatrix} H_{11} & H_{12} & \cdots & H_{1P} \\ H_{21} & H_{22} & \cdots & H_{2P} \\ \vdots & \vdots & \ddots & \vdots \\ H_{P1} & H_{P2} & \cdots & H_{PP} \end{bmatrix} \begin{bmatrix} \Gamma_1 \\ \Gamma_2 \\ \vdots \\ \Gamma_P \end{bmatrix} - \begin{bmatrix} \Upsilon_1 \\ \Upsilon_2 \\ \vdots \\ \Upsilon_P \end{bmatrix} = \begin{bmatrix} G_{11} & G_{12} & \cdots & G_{1P} \\ G_{21} & G_{22} & \cdots & G_{2P} \\ \vdots & \vdots & \ddots & \vdots \\ G_{P1} & G_{P2} & \cdots & G_{PP} \end{bmatrix} \begin{bmatrix} U_1 \\ U_2 \\ \vdots \\ U_P \end{bmatrix} \tag{25}$$

where

$$H_{pq} = -\frac{jk_0}{4}\int_C H_1^{(2)}\left(k_0\left|\vec{\rho}_q - \vec{\rho}'\right|\right)Q_p(\eta)\hat{n}\cdot\hat{r}\, d\eta + \delta_{qq} \tag{26}$$

and

$$G_{pq} = \frac{j}{4}\int_C H_0^{(2)}\left(k_0^2\left|\rho_q - \rho'\right|\right)Q_p(\eta)\, d\eta \tag{27}$$

The normal derivative of ψ_t is then obtained by solution of equation (25) for $[U]_C$ in terms of $[\Gamma]_C$ to get

$$[U]_C = [G]^{-1}[H][\Gamma]_C - [G]^{-1}[\Upsilon]_C \tag{28}$$

where $[U]_C$ and $[\Gamma]_C$ refer to unknown nodal amplitudes on curve C. With substitution of equation (28) into equation (14), the rightside of equation (5) reduces to

$$\oint_C T\nabla\psi_t\cdot\hat{n}\, dc = [D][G]^{-1}[H][\Gamma]_C - [D][G]^{-1}[\Upsilon]_C \tag{29}$$

From equations (11) and (29), equation (5) can be written in matrix form as

$$[B][\Gamma] - [D][G]^{-1}[H][\Gamma]_C = [D][G]^{-1}[\Upsilon]_C \tag{30}$$

and solved for $[\Gamma]$, which also includes additional $[\Gamma]_C$ terms. Then $[U]_C$ is determined by substitution of $[\Gamma]_C$ into equation (28). The scattered far field in the φ direction is then determined by the last two terms of equation (24) with $\rho_q = \rho$ and the asymptotic evaluations of the Hankel functions as $\rho \to \infty$

$$f_s = -\frac{k_0}{4}\left(\frac{2j}{\pi k_0\rho}\right)^{1/2} e^{-jk_0\rho}\sum_{p=1}^{P}\Gamma_p\int_C Q_p(\eta)e^{jk_0\rho'\cos(\varphi-\varphi')}\, d\eta$$
$$+\frac{j}{4}\left(\frac{2j}{\pi k_0\rho}\right)^{1/2} e^{-jk_0\rho}\sum_{p=1}^{P}U_p\int_C Q_p(\eta)e^{jk_0\rho'\cos(\varphi-\varphi')}d\eta \tag{31}$$

where (ρ', φ') is a function of η. For TM and TE incidence, respectively, the radar cross section is then obtained from

$$\left.\begin{aligned}\sigma_{2D} &= \text{limit}_{\rho \to \infty}\, 2\pi\, \rho\, \frac{|f_s|^2}{E_0^2} \\ \sigma_{2D} &= \text{limit}_{\rho \to \infty}\, 2\pi\, \rho\, \frac{|f_s|^2}{H_0^2}\end{aligned}\right\} \tag{32}$$

4. Numerical Results

In this section, numerical results for the scattering width of various 2-D material cylinders are presented. To solve equation (30), the matrices $[B]$, $[D]$, $[G]$, and $[H]$ must be determined. Matrices $[B]$ and $[D]$ are sparse matrices, and their elements are determined by equations (9) and (15), respectively. Matrices $[H]$ and $[G]$ are dense matrices, and their elements are determined by equations (26) and (27), respectively. Equations (26) and (27) are evaluated with the use of Gauss quadrature numerical integration. When $p = q$, the integration in equation (26) results in $H_{qq} = (\Theta_q/(2\pi))$, where Θ_q is the internal angle at the qth node shown in figure 3. The column matrix $[\Gamma]$, which is obtained after the solution of equation (30), is used in equation (28) to determine $[U]_C$. From known $[\Gamma]$ and $[U]_C$ on curve C, the scattered far field, and hence, the scattering width are determined by equations (31) and (32).

To validate the computer code, the bistatic scattering width of a perfectly conducting cylinder of radius 1.0λ, when excited by a TM-polarized plane wave, is calculated by the present formulation and compared with the calculated results given in reference 1. (See fig. 4.) Results of the two calculation methods are in good agreement. For calculations by the present method, the circular cylinder is assumed to be enclosed by an artificial circle with radius equal to 1.2λ. The region enclosed by the artificial circle is analyzed by the finite element method, and the region outside the circle is analyzed by the boundary element method. For the BEM the circle is divided into 76 points. Selection of the location of the artificial boundary around the cylinder is arbitrary. For the conducting cylinder, when the location of the artificial boundary coincides with the object boundary, the problem can be solved by the use of only BEM. For validation of the FEM formulation, the location of the artificial boundary was selected at 1.2λ radius to provide a minimum one-cell-thick FEM region. If the artificial boundary is moved farther away from the object boundary, the computational area is unnecessarily increased. The circumference of the artificial boundary was divided into 76 linear segments so that the length of each small segment was less than 0.1λ. In figure 5 the bistatic scattering width of the circular cylinder, when excited by a TE-polarized plane wave, is shown and compared with earlier published results. (See ref. 1.)

To check if dielectric and magnetic materials are properly handled by the present method, the bistatic scattering width of a material-coated circular cylinder is calculated for both TE and TM excitations and presented in figures 6–8 along with earlier published results. (See ref. 1.) Overall earlier results and the present method results are in good agreement. For the results presented in figures 6–8, the artificial circular boundary was taken at radius b. The artificial boundary was divided into 90 segments. Any further increase in the discretization of the artificial boundary C resulted in insignificant changes in the results presented in figures 6–8.

In general, the artificial boundary curve C enclosing the cylindrical scattering structure may be of any shape. To check this aspect, the bistatic scattering widths of cylinders with triangular cross sections, as shown in figure 9(a), are considered. The triangular cylinders are enclosed by the following boundaries: (1) circular boundary (fig. 9(a)), (2) elliptical boundary (fig. 9(b)), (3) conformal boundary with

blended corners (fig. 9(c)), and (4) conformal boundary with sharp corners (fig. 9(d)). The bistatic scattering widths, which were obtained for the four examples, are shown in figure 10 for comparison with earlier results published by Peterson and Castillo in reference 6. Results presented in figure 10 are in good agreement with each other. The results presented in figure 9 show advantages from the artificial boundary selected to be as close as possible to the outer boundary of the cylinder. This reduces the computational surface and, hence, the number of unknowns. For the examples considered, the artificial boundary selected in figure 9(d) is the optimum because it has the least number of unknowns when compared with the artificial boundaries considered in figures 9(a)–9(c).

Other geometries and their results are shown in figures 11–13. The geometries that were considered included the conducting strip shown in figure 11(a), the microstrip transmission line shown in figure 12(a), and the conducting cylinder of von Karman shape shown in figure 13(a). For the calculation of the scattering widths of a conducting strip, a microstrip transmission line, and a conducting cylinder of von Karman shape, the artificial boundaries were selected to be elliptical enclosures of the outer boundaries of the structures as shown in figures 11(a), 12(a), and 13(a), respectively. The scattering widths of these structures calculated by the present method are presented along with earlier published results (ref. 1) in figures 11(b), 11(c), 12(b), and 13(b). The results of all geometries are in good agreement.

5. Conclusion

A hybrid technique that combines the finite element method and boundary element method has been used to determine backscattered fields from arbitrarily shaped material cylinders. Validity of the computer code developed with the present hybrid technique has been demonstrated with various arbitrarily shaped material cylinders. Although use of the boundary element method in the present hybrid technique leads to a partly sparse and partly dense matrix, the present method is guaranteed to converge irrespective of the shape of the terminating or artificial boundary enclosing the arbitrarily shaped material cylinder. The present hybrid technique can be applied to study the transmission line characteristic of cylindrical strip lines.

NASA Langley Research Center
Hampton, VA 23681-0001
February 26, 1996

6. References

1. Arvas, Ercument; and Sarkar, Tapan K.: RCS of Two-Dimensional Structures Consisting of Both Dielectrics and Conductors of Arbitrary Cross Section. *IEEE Trans. Antennas & Propag.*, vol. 37, May 1989, pp. 546–554.

2. Richmond, J. H.: Scattering by a Dielectric Cylinder of Arbitrary Cross Section Shape. *IEEE Trans. Antennas & Propag.*, vol. AP-13, May 1965, pp. 334–341.

3. Sarkar, Tapan K.; and Arvas, Ercument: Scattering Cross Section of Composite Conducting and Lossy Dielectric Bodies. *IEEE Proc.*, vol. 77, May 1989, pp. 788–795.

4. Schaubert, D. H.; Wilton, D. R.; and Glisson, A. W.: A Tetrahedral Modeling Method for Electromagnetic Scattering Arbitrarily Shaped Inhomogeneous Dielectric Bodies. *IEEE Trans. Antennas & Propag.*, vol. AP-32, Jan. 1984, pp. 77–85.

5. Silvester, P. P.; and Ferrari, R. L.: *Finite Elements for Electrical Engineers*. Cambridge Univ. Press, 1990.

6. Peterson, Andrew F.; and Castillo, Steven P.: A Frequency-Domain Differential Equation Formulation for Electromagnetic Scattering From Inhomogeneous Cylinders. *IEEE Trans. Antennas & Propag.*, vol. 37, May 1989, pp. 601–660.

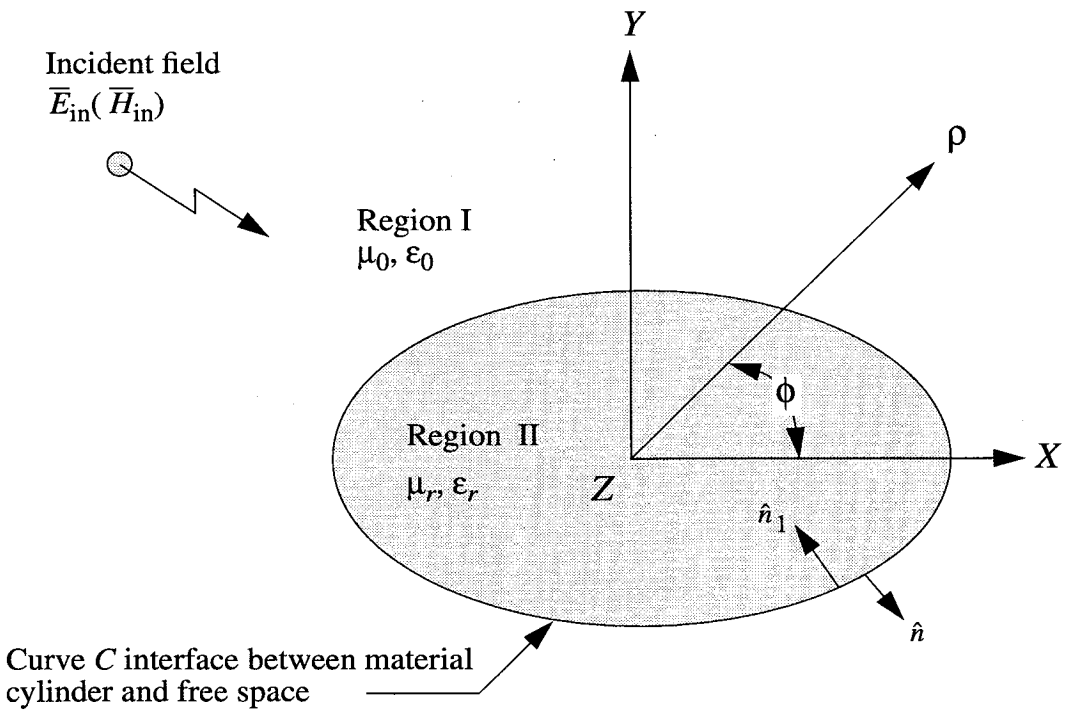

Figure 1. Material cylindrical scatterer and related coordinate system.

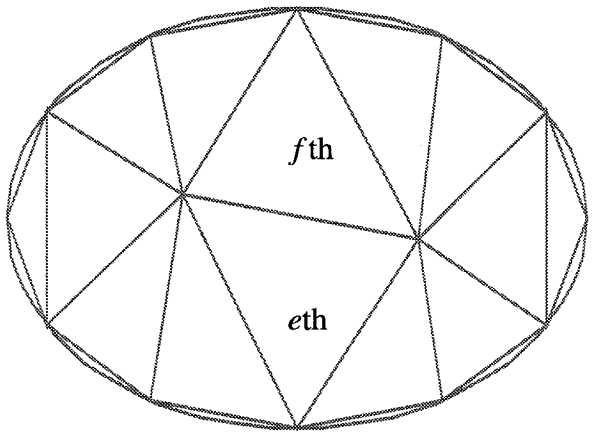

(a) Typical eth and fth triangles.

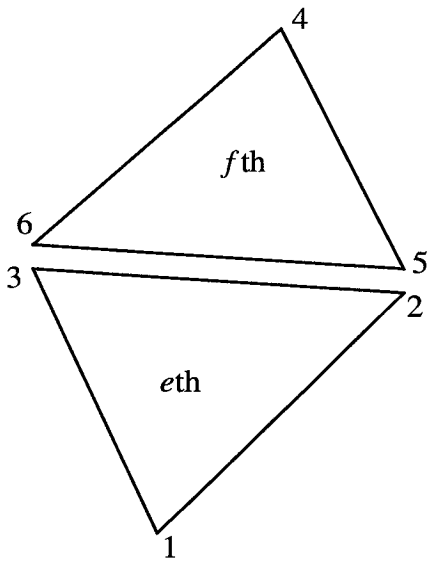

(b) Geometry of union of two triangles.

Figure 2. Region II discretized into triangular subdomains.

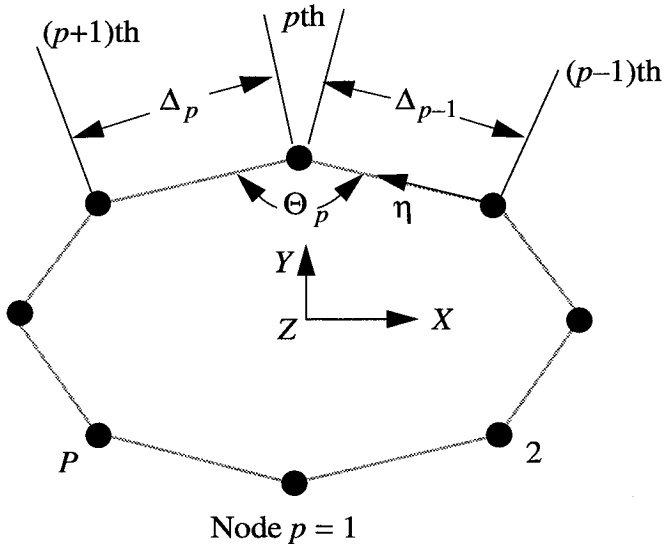

Figure 3. Geometry of discretized boundary curve C.

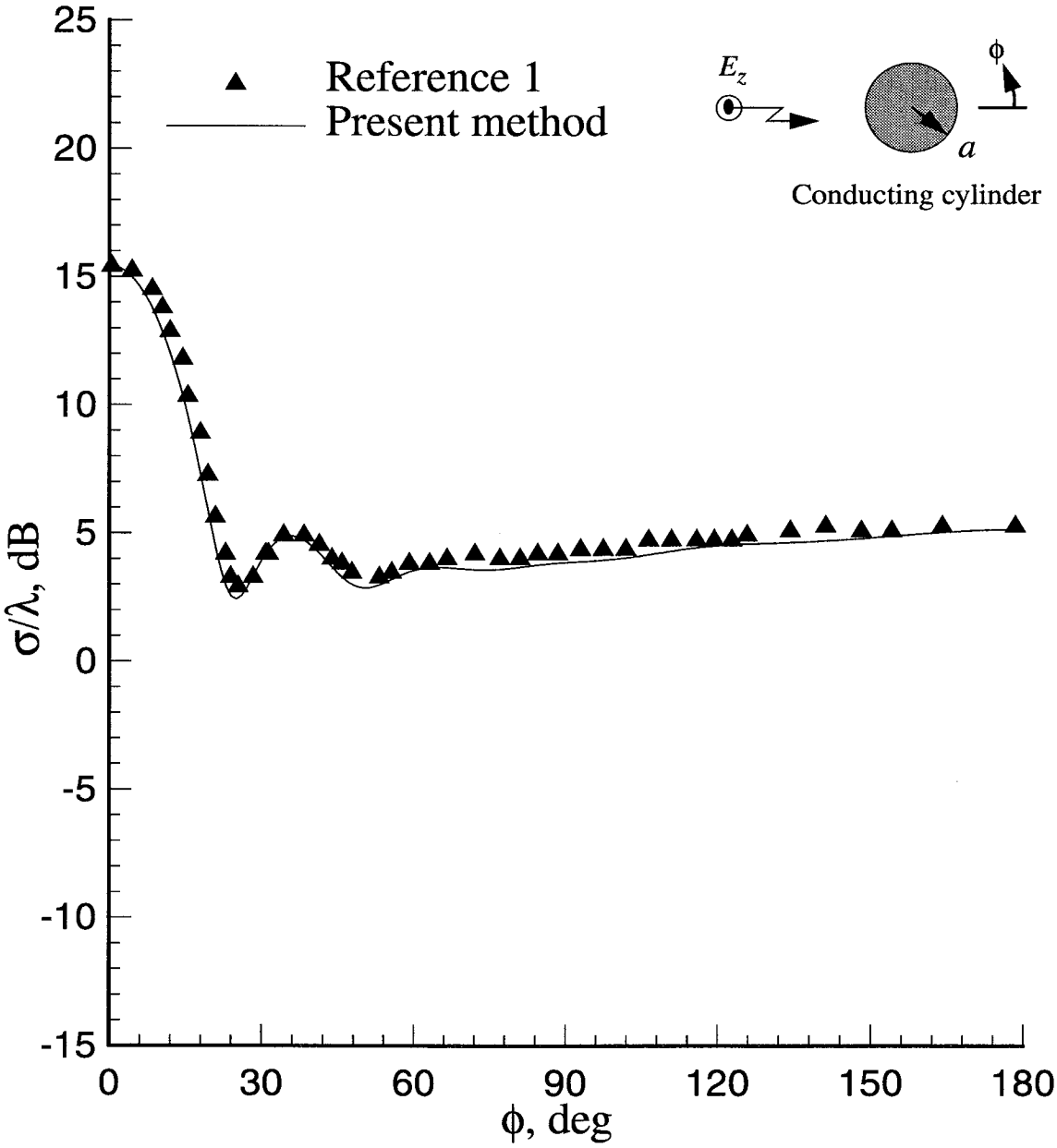

Figure 4. Bistatic scattering width of conducting circular cylinder excited by TM-polarized plane wave. $\alpha = 1.0\lambda$ and $\phi_{in} = 180°$.

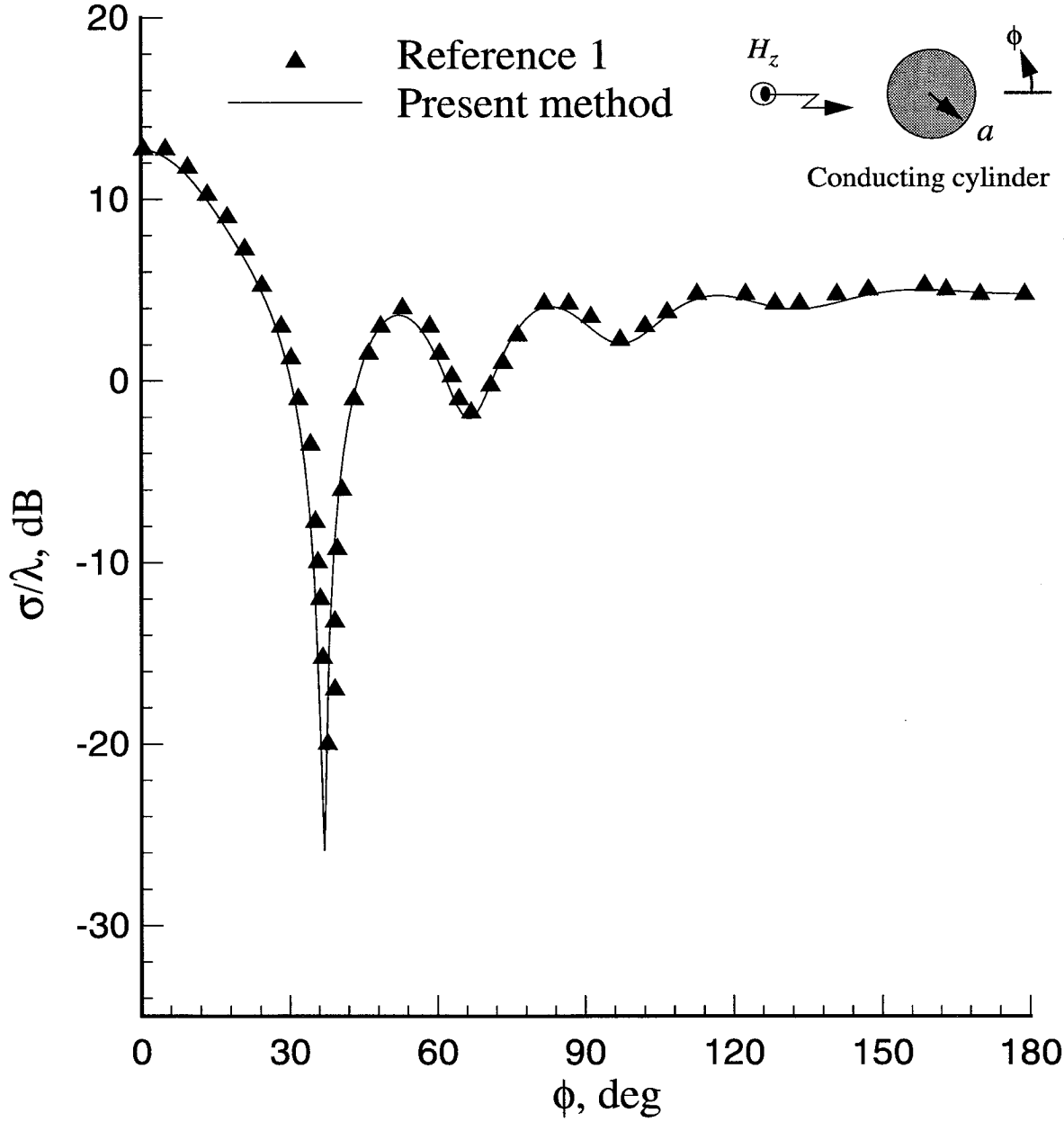

Figure 5. Bistatic scattering width of conducting circular cylinder excited by TE-polarized plane wave. $\alpha = 1.0\lambda$ and $\phi_{in} = 180°$.

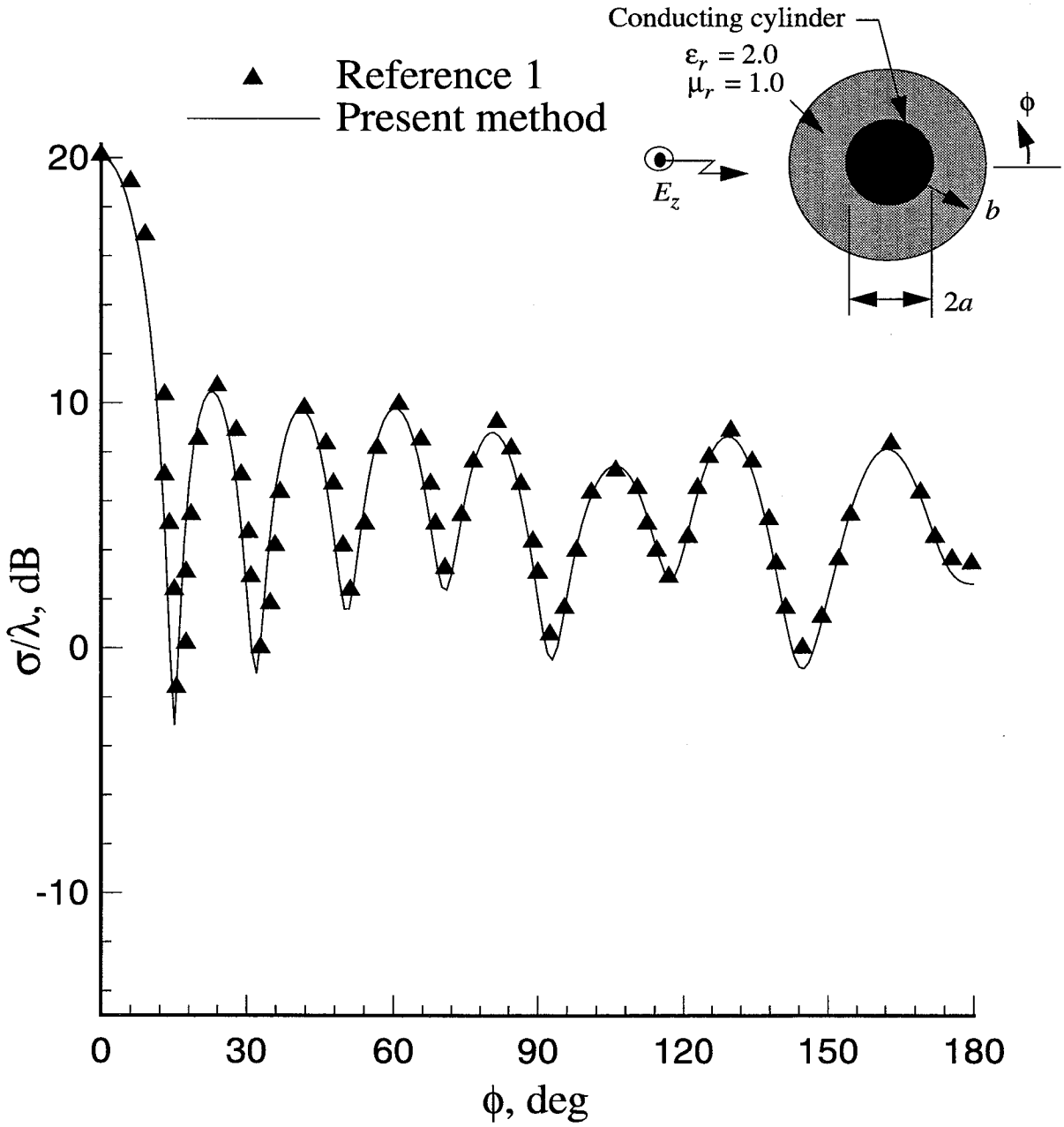

Figure 6. Bistatic scattering width of coated conducting circular cylinder excited by TM-polarized plane wave. $a = 1.0\lambda$; $b = 1.5\lambda$; $\varepsilon_r = 2.0$; $\mu_r = 1.0$; and $\phi_{in} = 180°$.

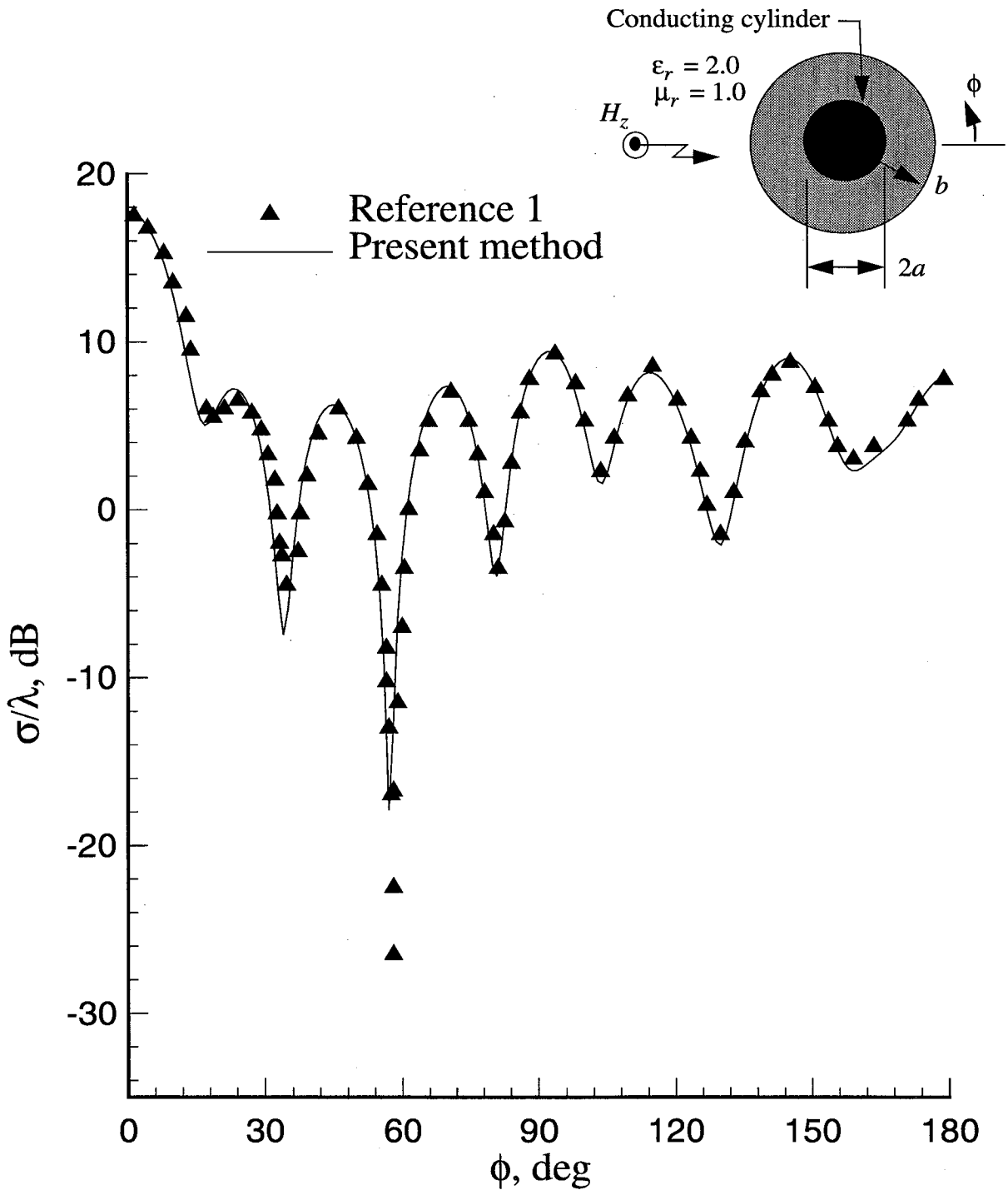

Figure 7. Bistatic scattering width of coated conducting circular cylinder excited by TE-polarized plane wave. $a = 1.0\lambda$; $b = 1.5\lambda$; $\varepsilon_r = 2.0$; $\mu_r = 1.0$; and $\phi_{in} = 180°$.

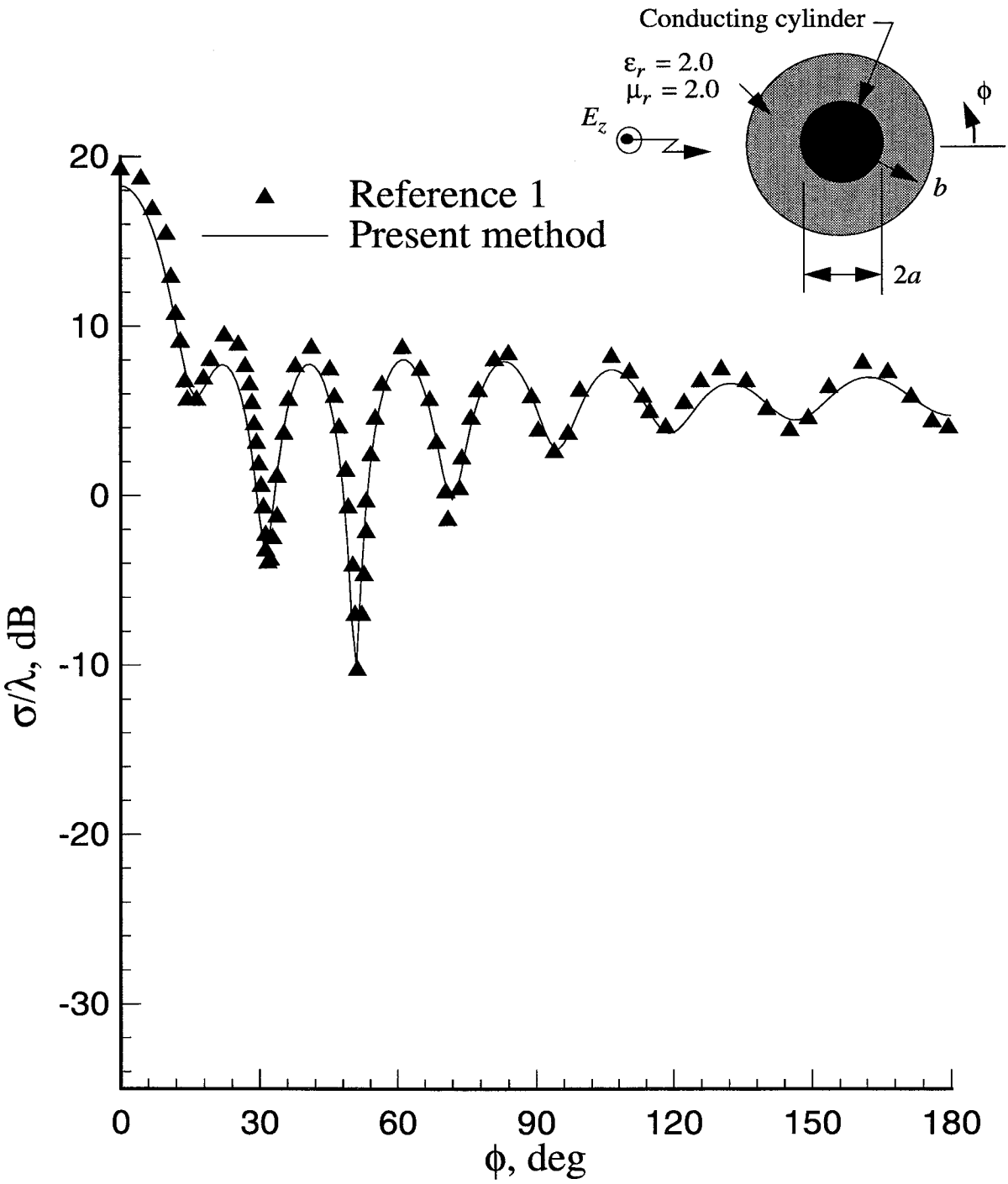

Figure 8. Bistatic scattering width of coated conducting circular cylinder excited by TE-polarized plane wave. $a = 1.0\lambda$; $b = 1.5\lambda$; $\varepsilon_r = 2.0$; $\mu_r = 2.0$; and $\phi_{in} = 180°$.

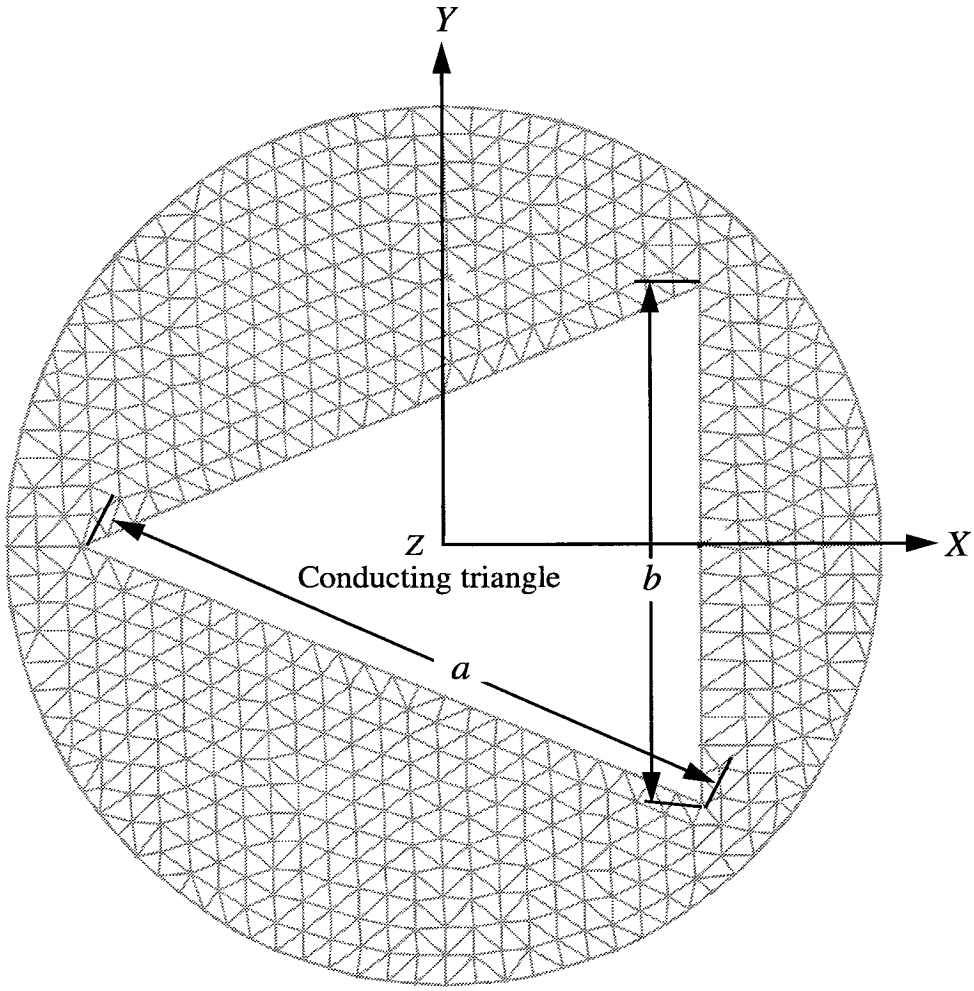

(a) Artificial circular boundary with radius $1.2\lambda_0$.

Figure 9. Isosceles triangular metallic cylinder with $a = 1.85\lambda_0$ and $b = 1.404\lambda_0$. FEM method is used inside circular boundary and BEM method is used outside circular boundary.

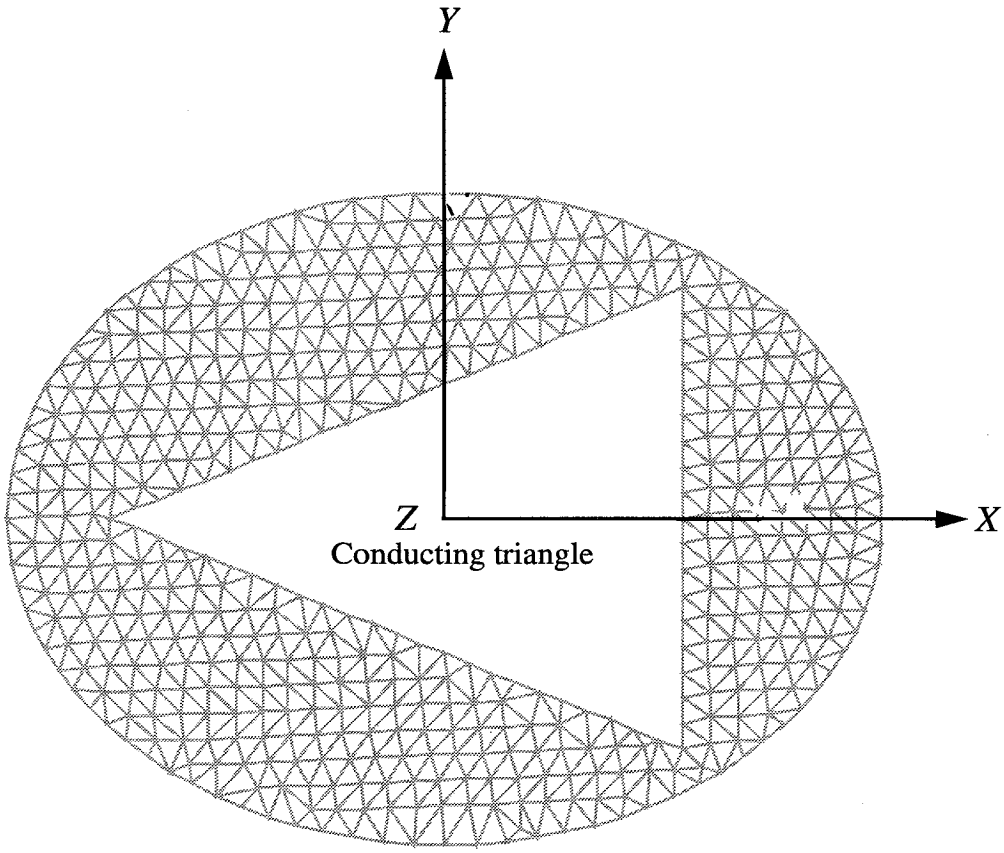

(b) Artificial elliptical boundary with major axis $1.3\lambda_0$ and minor axis $1.1\lambda_0$.

Figure 9. Continued.

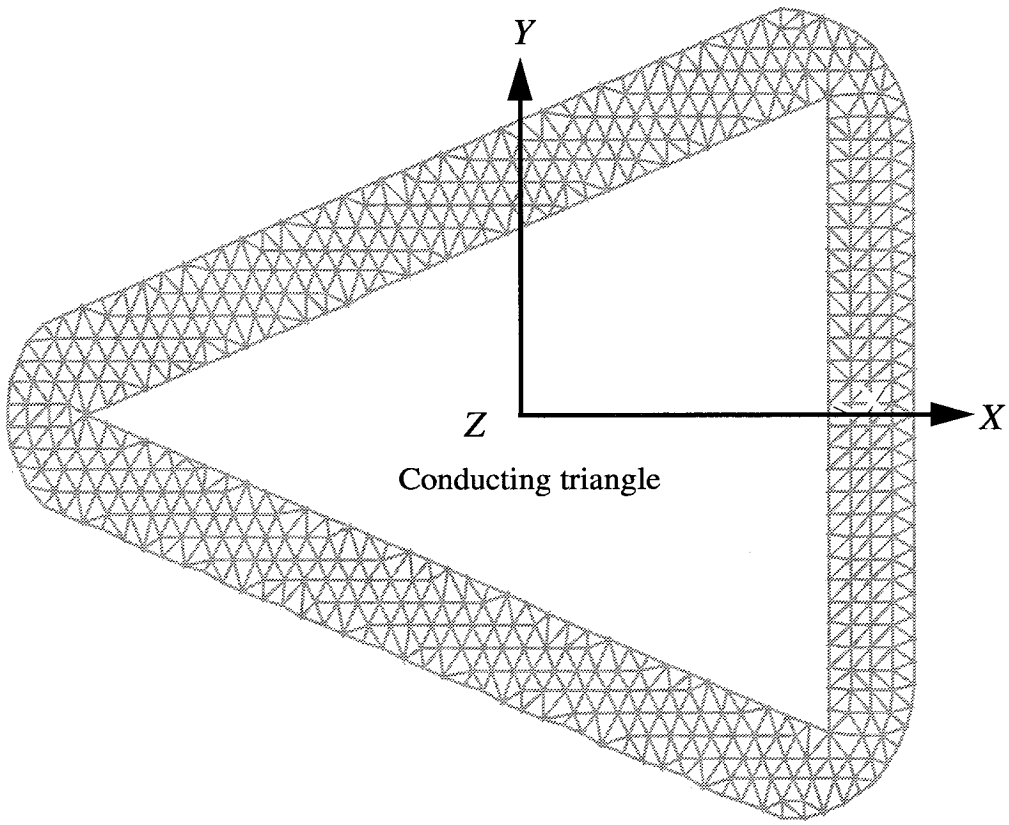

(c) Artificial conformal boundary with blended corners 3 to 4 cells away from triangle.

Figure 9. Continued.

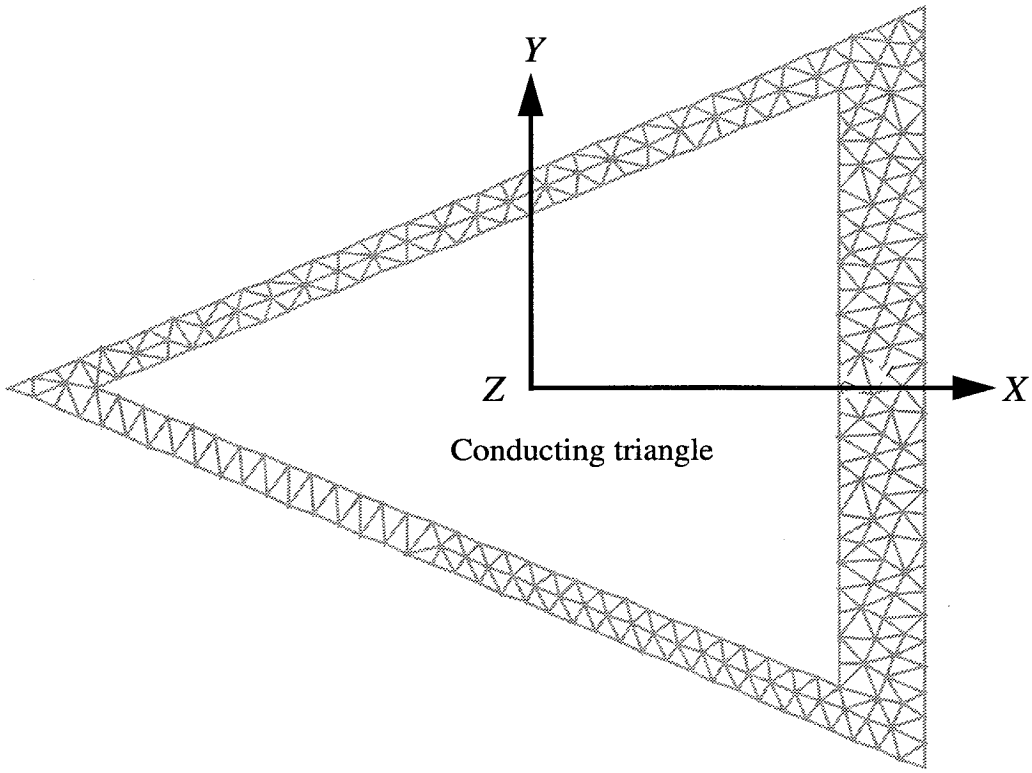

(d) Artificial conformal boundary with sharp corners 1 to 3 cells away from triangle.

Figure 9. Concluded.

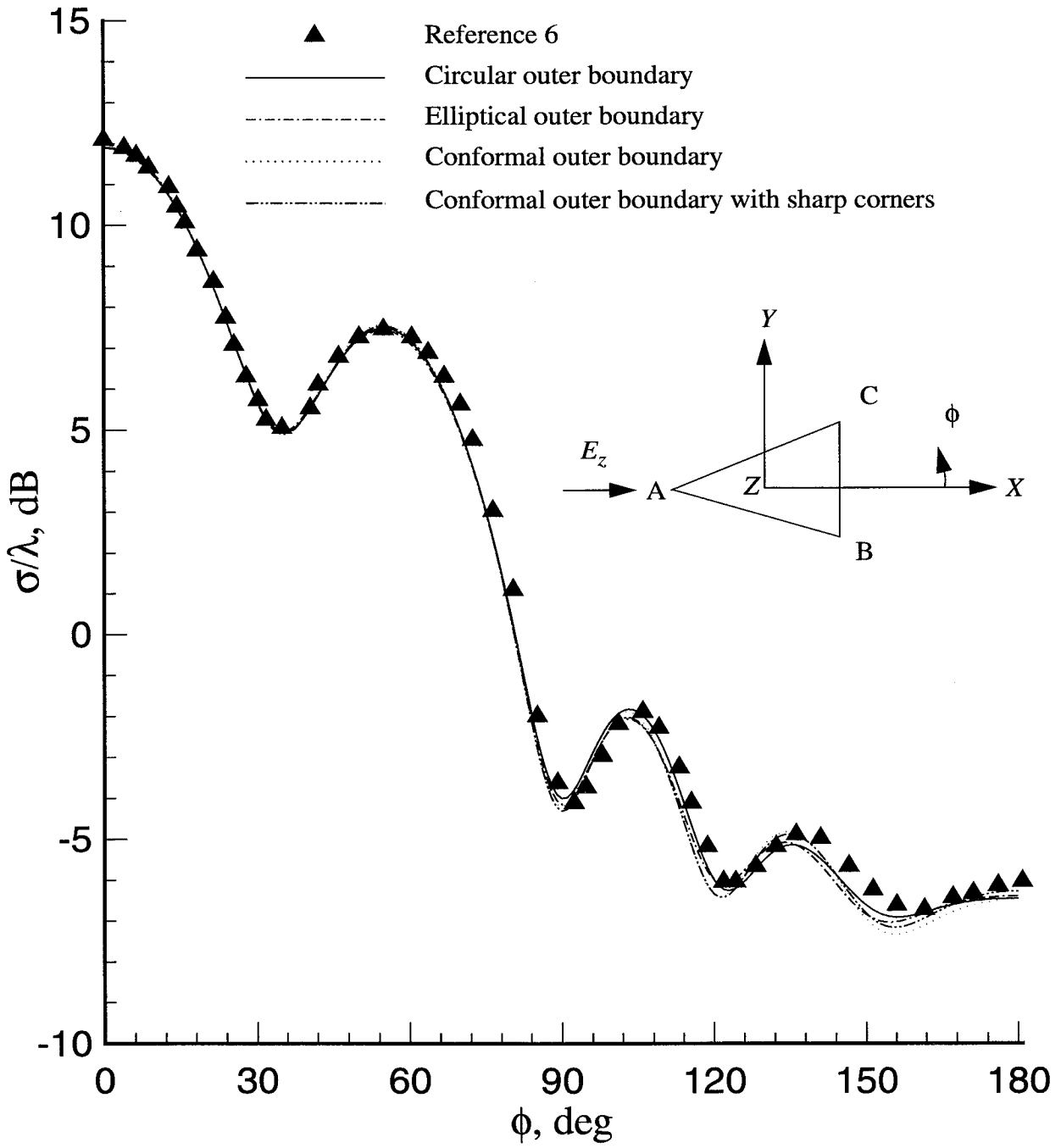

Figure 10. Bistatic scattering cross section of isosceles triangular cylinder shown in figure 9 and excited by TM-polarized plane wave with angle of incidence ϕ_{in} = 180°. Computed boundaries as shown in figure 9.

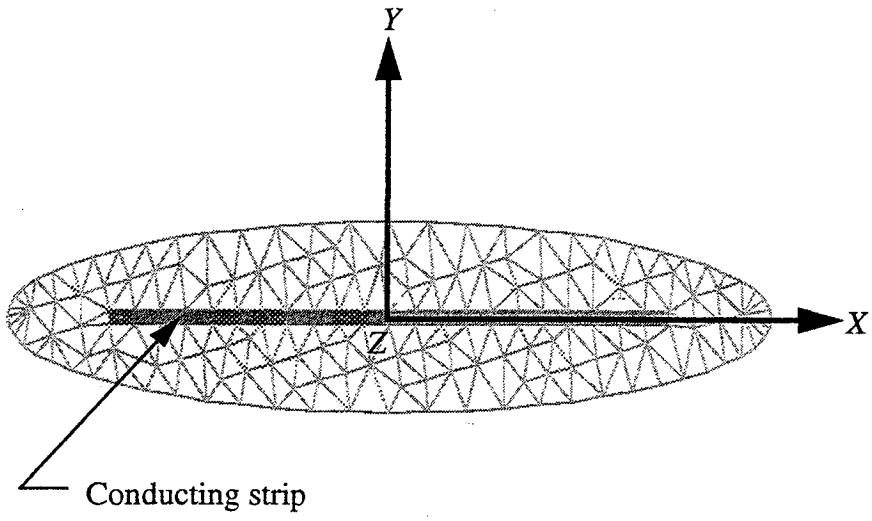

(a) Geometry and triangular mesh.

Figure 11. Conducting strip (infinite along Z-axis) with artificial elliptical boundary with major axis $1.3\lambda_0$ and minor axis $0.3\lambda_0$.

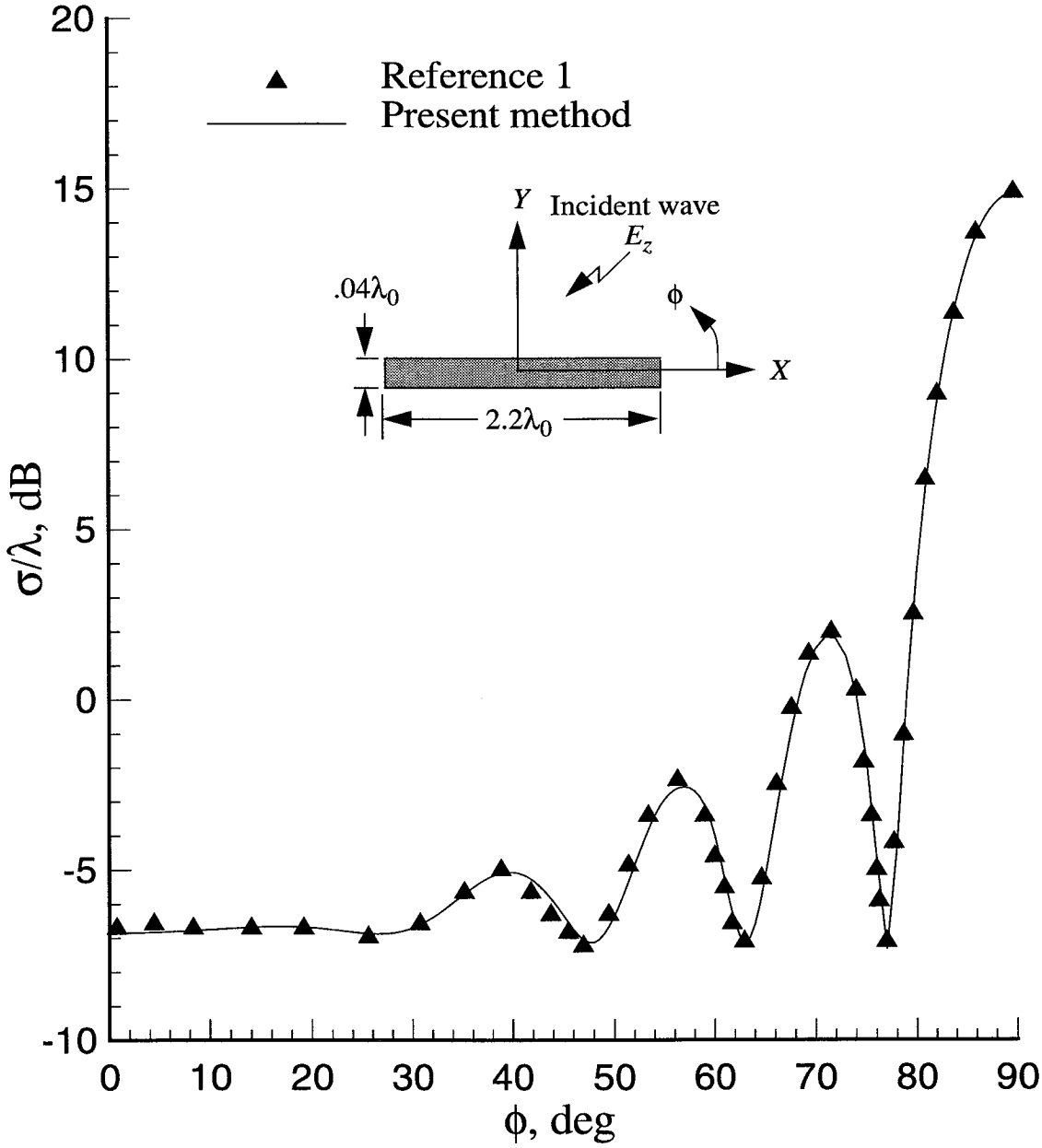

(b) Monostatic scattering width of conducting strip excited by TM-polarized plane wave.

Figure 11. Continued.

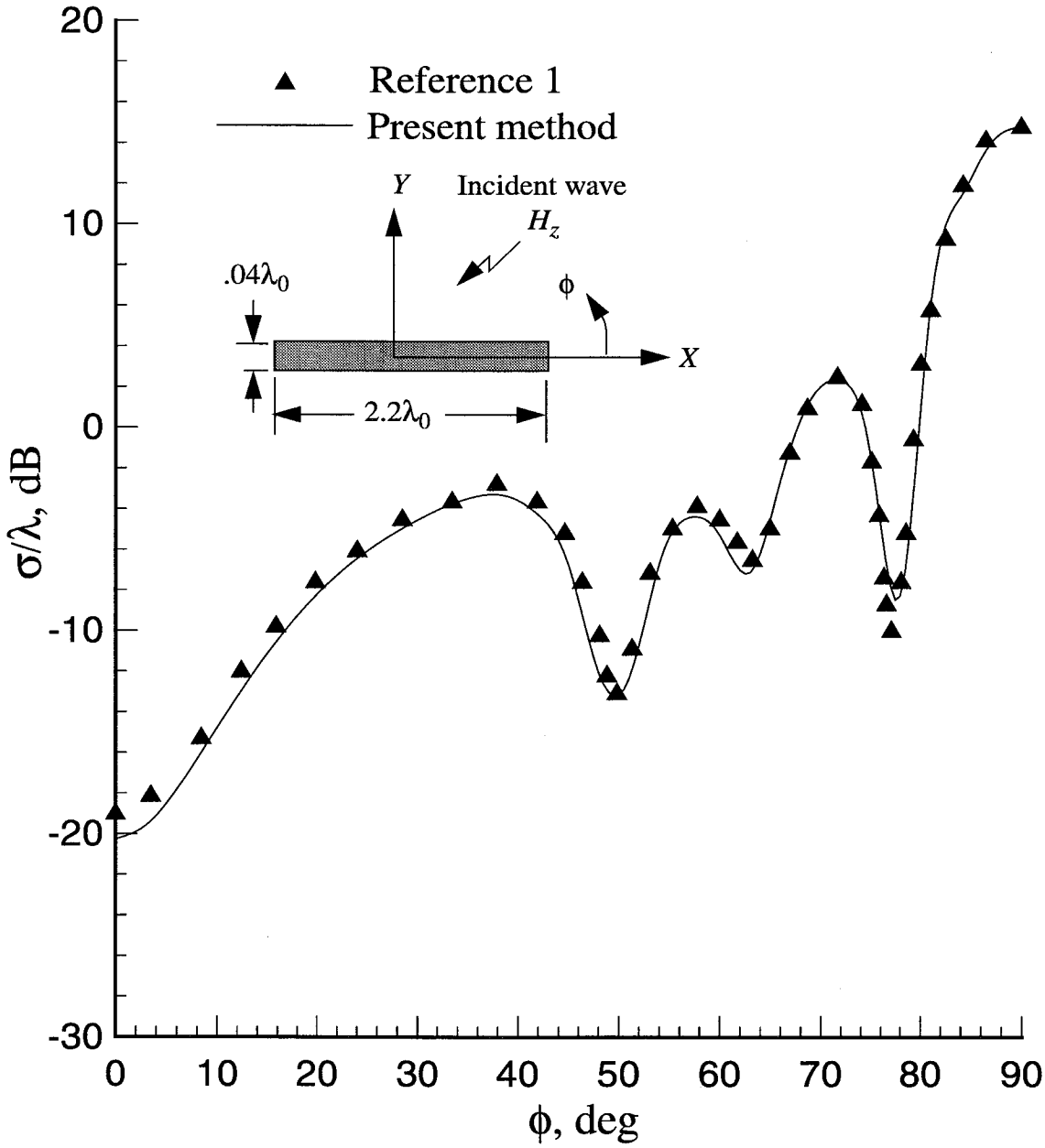

(c) Monostatic scattering width of conducting strip excited by TE-polarized plane wave.

Figure 11. Concluded.

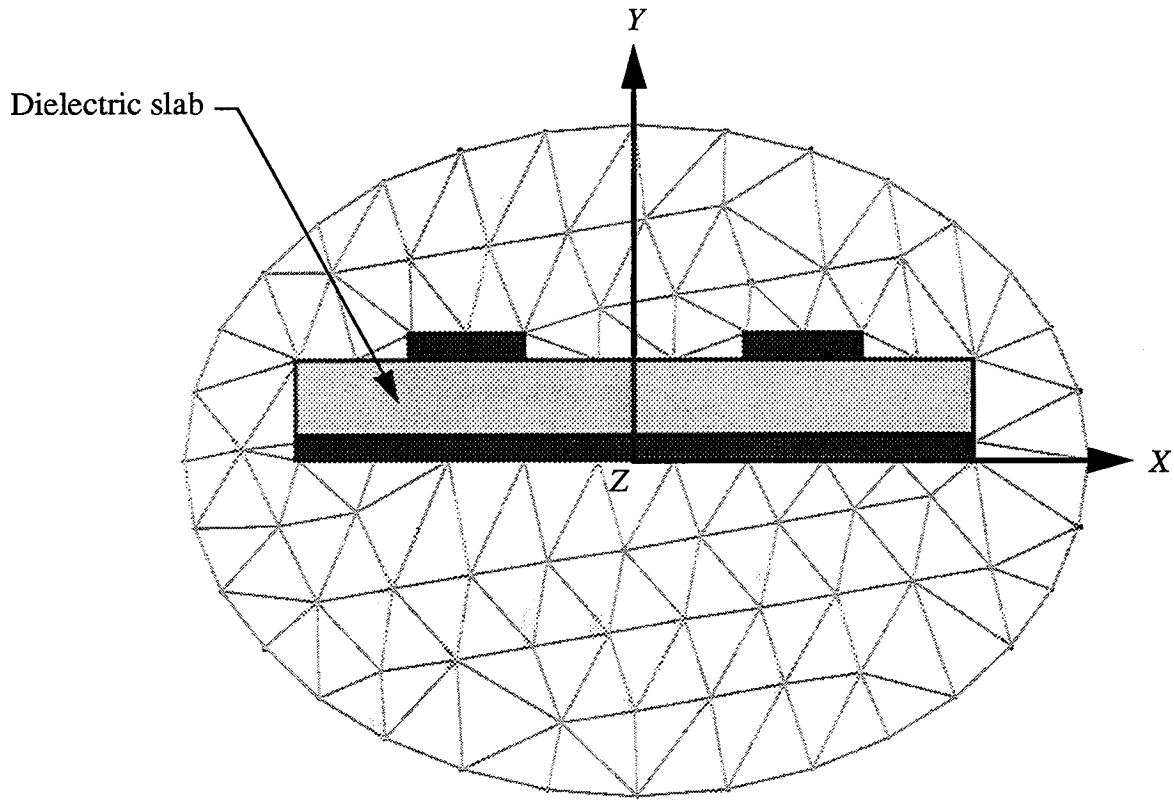

(a) Geometry and triangular mesh.

Figure 12. Microstrip transmission line with artificial elliptical boundary with major axis $0.6\lambda_0$ and minor axis $0.3\lambda_0$.

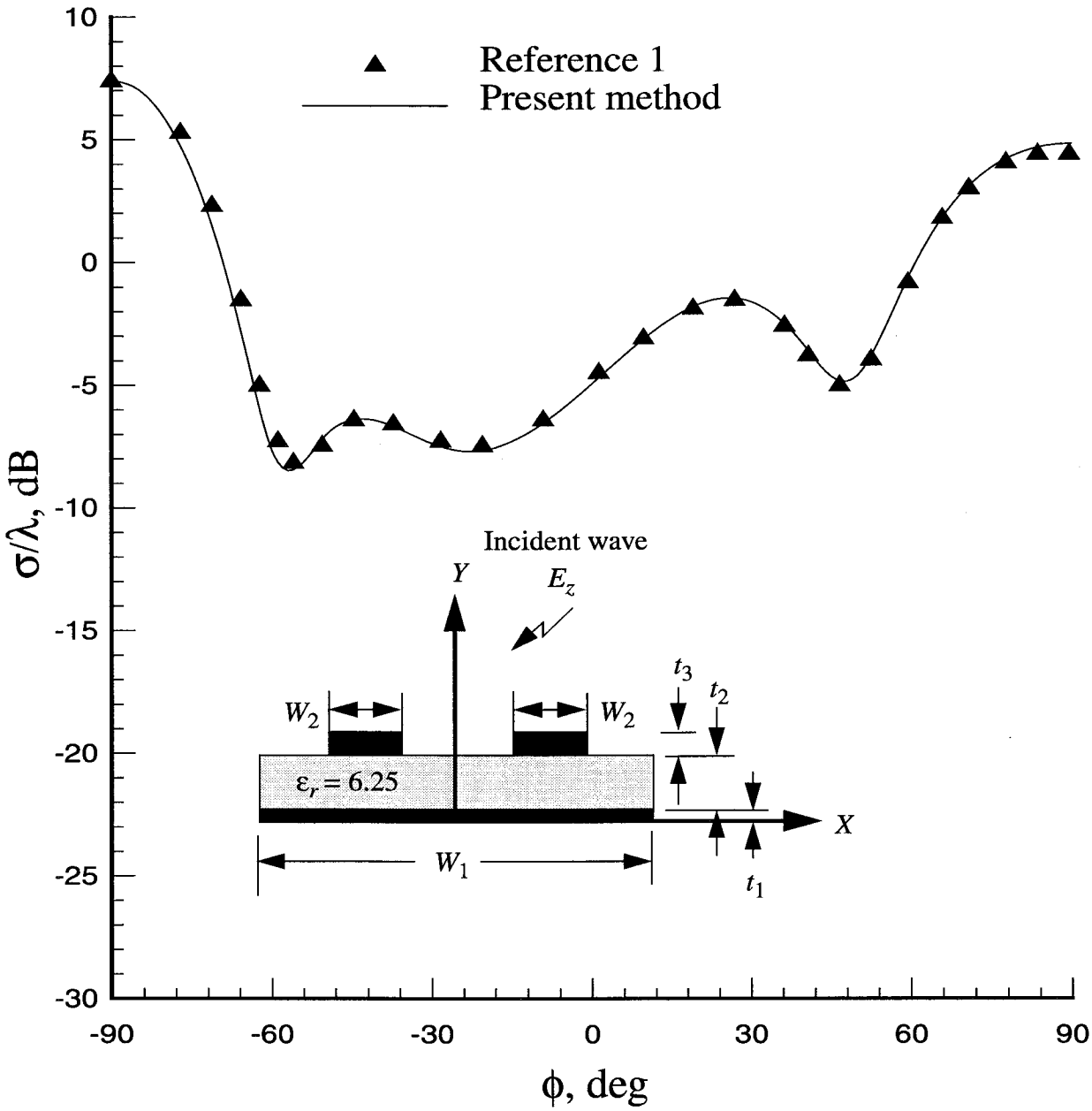

(b) Monostatic scattering width of microstrip transmission line excited by TM-polarized plane wave. $W_1 = 0.9\lambda_0$; $W_2 = 0.15\lambda_0$; $t_1 = 0.02\lambda_0$; $t_2 = 0.1\lambda_0$; and $t_3 = 0.05\lambda_0$.

Figure 12. Concluded.

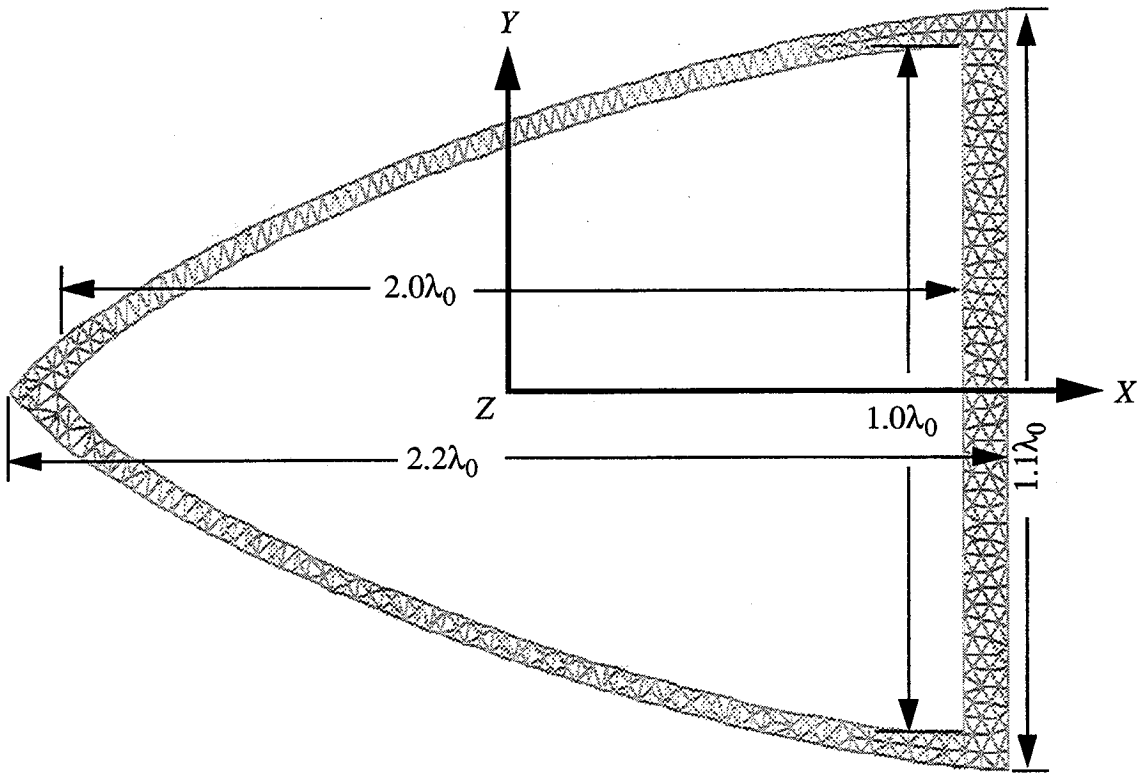

(a) Geometry and triangular mesh.

Figure 13. Conducting cylinder of von Karman shape with conformal artificial boundary.

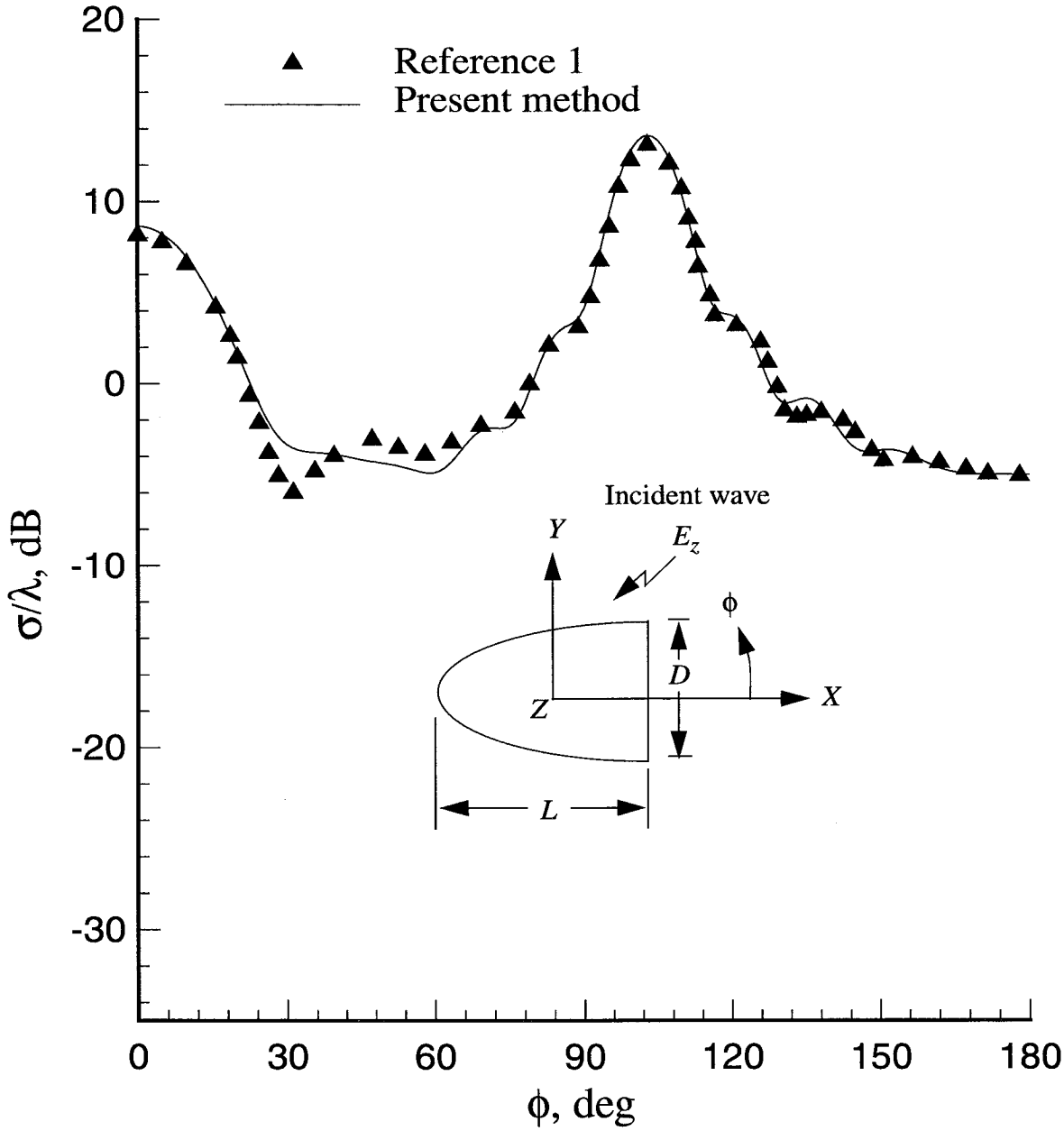

(b) Monostatic scattering width of conducting cylinder of von Karman shape excited by TM-polarized plane wave. $L = 2.0\lambda_0$ and $D = L/2$.

Figure 13. Concluded.

REPORT DOCUMENTATION PAGE

Form Approved
OMB No. 0704-0188

1. AGENCY USE ONLY *(Leave blank)*	2. REPORT DATE	3. REPORT TYPE AND DATES COVERED
	July 1996	Technical Paper

4. TITLE AND SUBTITLE
Electromagnetic Scattering Analysis of Arbitrarily Shaped Material Cylinder by FEM-BEM Method

5. FUNDING NUMBERS
WU 505-64-52-04

6. AUTHOR(S)
M. D. Deshpande, C. R. Cockrell, and C. J. Reddy

7. PERFORMING ORGANIZATION NAME(S) AND ADDRESS(ES)
NASA Langley Research Center
Hampton, VA 23681-0001

8. PERFORMING ORGANIZATION REPORT NUMBER
L-17469

9. SPONSORING/MONITORING AGENCY NAME(S) AND ADDRESS(ES)
National Aeronautics and Space Administration
Washington, DC 20546-0001

10. SPONSORING/MONITORING AGENCY REPORT NUMBER
NASA TP-3575

11. SUPPLEMENTARY NOTES
Deshpande: ViGYAN, Inc., Hampton, VA; Cockrell: Langley Research Center, Hampton, VA; Reddy: NRC-NASA Resident Research Associate, Langley Research Center, Hampton, VA.

12a. DISTRIBUTION/AVAILABILITY STATEMENT
Unclassified–Unlimited
Subject Category 17
Availability: NASA CASI (301) 621-0390

12b. DISTRIBUTION CODE

13. ABSTRACT *(Maximum 200 words)*
A hybrid method that combines the finite element method (FEM) and the boundary element method (BEM) is developed to analyze electromagnetic scattering from arbitrarily shaped material cylinders. By this method, the material cylinder is first enclosed by a fictitious boundary. Maxwell's equations are then solved by FEM inside and by BEM outside the boundary. Electromagnetic scattering from several arbitrarily shaped material cylinders is computed and compared with results obtained by other numerical techniques.

14. SUBJECT TERMS
Electromagnetic scattering; Hybrid FEM-BEM technique

15. NUMBER OF PAGES
31

16. PRICE CODE
A03

17. SECURITY CLASSIFICATION OF REPORT	18. SECURITY CLASSIFICATION OF THIS PAGE	19. SECURITY CLASSIFICATION OF ABSTRACT	20. LIMITATION OF ABSTRACT
Unclassified	Unclassified	Unclassified	